Elaboration of Superparamagnetic Cobalt–Ferrite Nanocomposites from Films of Chitosan Chelates

M. A. Garza-Navarro,[1,2] V. A. González-González,[1,2] A. Torres-Castro,[1,2] M. Hinojosa,[1,2] A. García-Loera,[1,2] M. José-Yacamán[3]

[1]*Facultad de Ingeniería Mecánica y Eléctrica, Universidad Autónoma de Nuevo León, Universidad Avenida S/N, San Nicolás de los Garza, Nuevo León 66450, Mexico*
[2]*Centro de Innovación, Investigación y Desarrollo en Ingeniería y Tecnología, Nueva Autopista al Aeropuerto Mariano Escobedo Kilómetro 10, Apodaca, Nuevo León 66600, Mexico*
[3]*Physics and Astronomy Department, University of Texas at San Antonio, 1 UTSA Circle, San Antonio, Texas 78249-1644*

Received 16 January 2009; accepted 28 June 2009
DOI 10.1002/app.31043
Published online 26 March 2010 in Wiley InterScience (www.interscience.wiley.com).

ABSTRACT: Cobalt–ferrite nanocomposites were synthesized from polymeric films of chelates of Co(II) and Fe(III) ions within a chitosan matrix by a solid-state coprecipitation reaction with weight content ratios of chitosan to cobalt–ferrite of 50/50 and 25/75 w/w. Morphological and crystalline studies of the composites were performed by high-resolution transmission electron microscopy, X-ray diffraction, and selected area electron diffraction with a nanobeam diffraction probe. The results show nanoparticles around 4 nm with a spinel structure, consistent with the cobalt–ferrite phase. The magnetic behavior was evaluated with curves of the applied-field-dependent magnetization [$M(H)$] and the temperature-dependent magnetization [$M(T)$]. Both the $M(H)$ and $M(T)$ curves showed typical superparamagnetic behavior, depicting an absence of hysteretic characteristics and the characteristic peak at blocking temperature in the zero-field-cooled curve. There was also evidence of strong interparticle and intraparticle interactions, which suggested magnetic frustration in the particle magnetic moment alignment with the applied field. © 2010 Wiley Periodicals, Inc. J Appl Polym Sci 117: 785–792, 2010

Key words: biopolymers; magnetic polymers; nanocomposites

INTRODUCTION

The synthesis of magnetic nanoparticles of spinel oxides has attracted attention over the years because these particles present remarkable potential applications in many technological areas, such as medicine, biology, and electronics.[1–9] The magnetic properties of such nanoparticles strongly depend on their dimensions. Below a certain size, they become a single domain and are capable of experiencing superparamagnetic relaxation phenomena above a critical temperature, known as the *blocking temperature.*[10] In addition, important surface effects can be present as the particle size is reduced, which can induce significant magnetic frustration over the alignment of the magnetic moment of the particles.[11,12] Moreover, in highly concentrated magnetic systems, it is possible to observe important interparticle interactions, which can also induce frustration phenomena in the response of the magnetic moment of the particles.[13]

Different successful routes have been used for the synthesis of different spinel oxides nanoparticles with methodologies such as microemulsion (micelles),[14,15] the polyol method,[16] and chemical coprecipitation[17–19] with either organic dissolvents or polymeric matrices as stabilizing media. Accordingly, the development of magnetic composites from spinel ferrite nanoparticles stabilized in organic matrices has been successfully reached by the use of polymers such as poly(vinyl alcohol),[20] poly(styrene-*b*-ethylene/butylene-*b*-styrene),[21] poly(styrenesulfonate),[22] and chitosan.[23] Among these matrices, polyamine–saccharide chitosan has been reported as a good candidate for the development of biomedical composite materials,[23–25] such as magnetic drug carriers and magnetic hyperthermia inductors. For example, the synthesis of chitosan/magnetite nanocomposites has been performed by a two-step procedure: first, the magnetite nanoparticles are synthesized by either sonochemical or traditional coprecipitation; next, they are dispersed in acid chitosan dissolutions.[25–29] Chitosan/magnetite nanocomposites have also been obtained by the coprecipitation of both ferric and ferrous ions, and chitosan has been obtained from acetic acid dissolutions to

Correspondence to: V. A. González-González (virgilio.gonzalezgnz@uanl.edu.mx).

Contract grant sponsors: Universidad Autónoma de Nuevo León, University of Texas at San Antonio, Consejo Nacional de Ciencia y Tecnología.

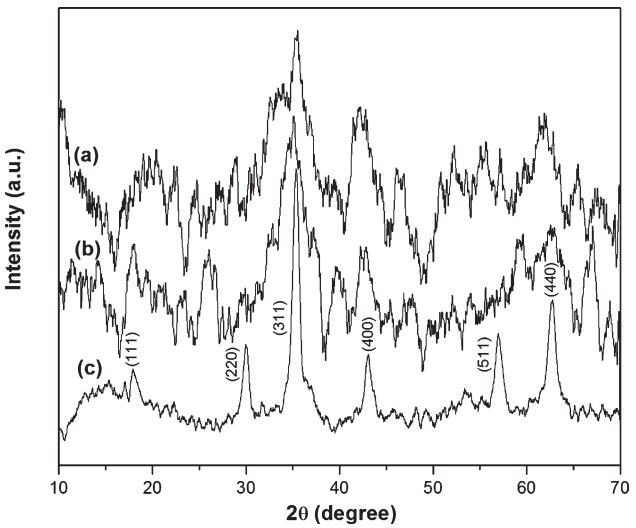

Figure 1 XRD patterns obtained from (a) 50/50CCF, (b) 25/75CCF, and (c) 100CF.

obtain chitosan/magnetite beads with magnetite concentrations in the range 5–20 wt %.[30,31] Moreover, it has been reported that chitosan presents a remarkable ability to form chelates with both divalent and trivalent transition-metal ions because of the amine functional groups of this biopolymer.[32–34]

In this article, we propose the synthesis of chitosan/cobalt–ferrite composites from chitosan polymeric films of chelates of Co(II) and Fe(III) ions by a one-step procedure consistent with an *in situ* solid-state coprecipitation reaction of these ions with the chitosan matrix as a template.

EXPERIMENTAL

Hexahydrated cobalt and thetrahydrated ferrous chlorides were dissolved in formic acid (88%) to give a stoichiometric ratio of 2 : 1 of Fe(III) to Co(II) under magnetic stirring at room conditions. The dissolution was mixed with a previously prepared dissolution of chitosan (Sigma-Aldrich with 84.5% desacetylation) in formic acid at concentration of 10.0 mg/mL. The amounts of each dissolution were mixed in the necessary proportions to obtain chitosan/cobalt–ferrite samples with weight content ratios of 50/50 and 25/75 w/w, which were identified as 50/50CCF and 25/75CCF, respectively. The dissolutions were placed in Petri dishes, and the dissolvent was evaporated in a vacuum chamber. The resulting yellowish films were immersed in a 5*M* aqueous dissolution of NaOH. The films turned dark brown, which indicated the *in situ* coprecipitation of the oxide. The films were then washed several times with deionized water and finally dried at room temperature.

In addition, nonstabilized cobalt ferrite was prepared from both hexahydrated cobalt and thetrahydrated ferrous chlorides dissolved in formic acid in the absence of chitosan dissolution. The precipitation process was performed by the addition of NaOH aqueous dissolution to the chloride dissolution at the necessary proportion until a dark precipitant was produced under a controlled pH reaction at room conditions. The resulting precipitant was washed several times with deionized water and dried overnight at 70°C. This sample was identified as 100CF.

Powdered samples were analyzed by X-ray diffraction (XRD) with a Bruker advanced X-ray solutions diffractometer with Cu Kα radiation (wavelength = 0.154 nm). Transmission electron microscopy was performed with a JEOL 2010F instrument at 200.0 kV. The specimens were prepared by dispersion of the chitosan/cobalt–ferrite powder in isopropyl alcohol with an ultrasonic bath and placement of an aliquot of the dispersion onto a lacey carbon-coated grid. Electron diffraction patterns were obtained in a JEOL 2010 with the nanobeam diffraction mode at probe sizes of 2 and 5 nm. Magnetic measurements of the samples were obtained with a MPMS SQUID-VSM magnetometer (Quantum Design).

RESULTS AND DISCUSSION

XRD patterns of the synthesized samples are shown in Figure 1. The position of peaks corresponding to the reflecting planes confirmed that the precipitated particles had the spinel structure reported for cobalt–ferrite (see JCPDS 22-1086 diffraction card). The interplanar spacing of the indexed reflecting peaks is summarized in Table I. The peak width tended to increase as the polymer content increased,

TABLE I
Interplanar Spacing Measurements Obtained from XRD, HRTEM, and Selected Area Electron Diffraction

Interplanar distance[a]	Experimental d_{hkl} (Å)[b]			Miller index
	XRD pattern	HRTEM imaging	Electron diffraction pattern	
2.97	2.98	2.91	2.85	(220)
2.53	2.53	2.50	2.52	(311)
2.42	—	—	2.38	(222)
2.10	2.10	—	2.09	(400)
1.71	—	—	1.77	(422)
1.62	1.61	—	1.63	(511)
1.48	1.48	—	1.45	(440)
1.42	—	—	1.42	(531)
1.28	—	—	1.28	(533)
1.09	—	—	1.08	(731)
1.05	—	—	1.05	(800)
0.97	—	—	0.10	(751)

[a] The interplanar spacing is reported in the JCPDS 22-1086 diffraction card.
[b] ±2%.

which could be related to a reduction in the crystal size as a function of the chitosan content. Nevertheless, to clearly observe this feature, it was necessary to estimate the crystal size by the Scherrer equation:

$$L = \frac{K\lambda}{\beta \cos \theta} \quad (1)$$

where L is the volume-weighted average crystal size, K is the Scherrer factor (taken as 0.90), λ is the X-ray wavelength (0.154 nm in our case), β is the mean width of the maximum peak, and θ is the Bragg angle of diffraction. The results of these calculations are shown in Table II, along with the corresponding unit cell parameter. From these results, one can see that the crystal size decreased significantly from the nonstabilized cobalt–ferrite sample (100CF) to the stabilized ones. Therefore, this variation could be associated with a stabilization feature of the chitosan matrix. To provide an explanation of the physical meaning of this variation, we proceeded to analyze the crystalline characteristics of the synthesized cobalt–ferrite particles.

Figure 2 shows high-resolution micrographs obtained by transmission electron microscopy for the chitosan-stabilized nanoparticles. Figure 2(a) shows the presence of several cobalt–ferrite nanoparticles embedded in the chitosan matrix, in this case from the sample 50/50CCF. Figure 2(b) shows the selected zone image where the morphology presented by the cobalt–ferrite nanoparticles is clear. Figure 2(c) shows a high-resolution micrograph of a zone selected from Figure 2(b), and subsequently, Figure 2(d) shows the Fourier transform filtered image from the zone indicated in Figure 2(c). In this image, a crystalline arrangement of atoms is shown, which is attributed to the spinel phase crystalline plane (220),[33] as the performed interplanar spacing measurements suggest. The inset shows its corresponding indexed Fourier transform image, which indicates that the crystalline structure corresponds to a spinel phase because the identified spots suggest a face-centered, cubic arrangement of anions. The crystalline orientation of the zone shown in Figure 2(d) with respect the electron beam is given by the vector **B.**

TABLE II
Crystal Sizes and Unit Cell Parameters Calculated from the XRD Patterns

Sample	Crystal size (nm)	Unit cell parameter (nm)
100CF	11.31 ± 1.67	0.8394
25/75CCF	4.96 ± 2.04	0.8411
50/50CCF	3.33 ± 1.18	0.8419

Figure 2(e) shows a nanoparticle from the sample 25/75CCF. Here, an atomic plane arrangement was also noticeable, which, as Figure 2(f) suggests, was attributed to the crystalline planes (220) and (311), as the interplanar spacing measurements indicated. The indexed Fourier transform image corroborates that the crystalline arrangement corresponds to a spinel phase, which is attributed to the cobalt–ferrite. The interplanar spacing measurements are compared with those reported for cobalt-ferrite in the Table I.

As is noticeable in the high-resolution transmission electron microscopy (HRTEM) images, the nanoparticles exhibited a regular array of crystalline planes, which did not present any disruption associated with crystalline faults (e.g., grain boundaries). Considering this observation, we were assured that the cobalt ferrite nanoparticles were single crystals and that their particle size was proportional to the size of their crystalline domains. Under this reasoning, the variation of the crystal size as a function of the chitosan content could be physically explained. Considering the synthesis route used, we expected that the particle size was controlled mainly by two factors: (1) the reactants' concentration and (2) the steric effect of the stabilization media, given by intermolecular sites used to nucleate the nanoparticles. Therefore, if the concentration of the reactants was controlled to obtain composites with a given cobalt–ferrite nanoparticle content, the final dimensions of the particles were governed by the size of the intermolecular sites where they grew.

Electron diffraction patterns of the composite sample are shown in Figure 3. Figure 3(a) displays the electron diffraction pattern of a nanoparticle from the sample 50/50CCF, where the observed spots are attributed to the (440), (422), and (511) reflecting planes of the cobalt–ferrite spinel phase. In addition, Figure 3(b) shows that the indexed spots correspond to the planes (220), (440), (311), and (333). The interplanar distances calculated from these diffraction patterns were also compared with those reported for each plane and are summarized in Table I.

Figure 4 shows the applied-field-dependent magnetization [$M(H)$] hysteresis loops for samples 25/75CCF and 50/50CCF obtained at different temperatures after a zero-field-cooled (ZFC) process. At 1.8 K, both samples, 25/75CCF and 50/50CCF, exhibited typical ferromagnetic behavior and showed coercivities of 1.21 and 1.34 T, remanence ratios of 0.30 and 0.32, and magnetization saturations of 61.50 and 65.53 A m^2/kg, respectively, which was deduced from linear extrapolation to an infinite field. In both cases, the remanence ratio was much smaller than that attributed to isolated particles with uniaxial anisotropy (0.5) or cubic anisotropy (0.8),[34–36] which suggested that in the magnetic system there was significant interparticle or intraparticle interaction,

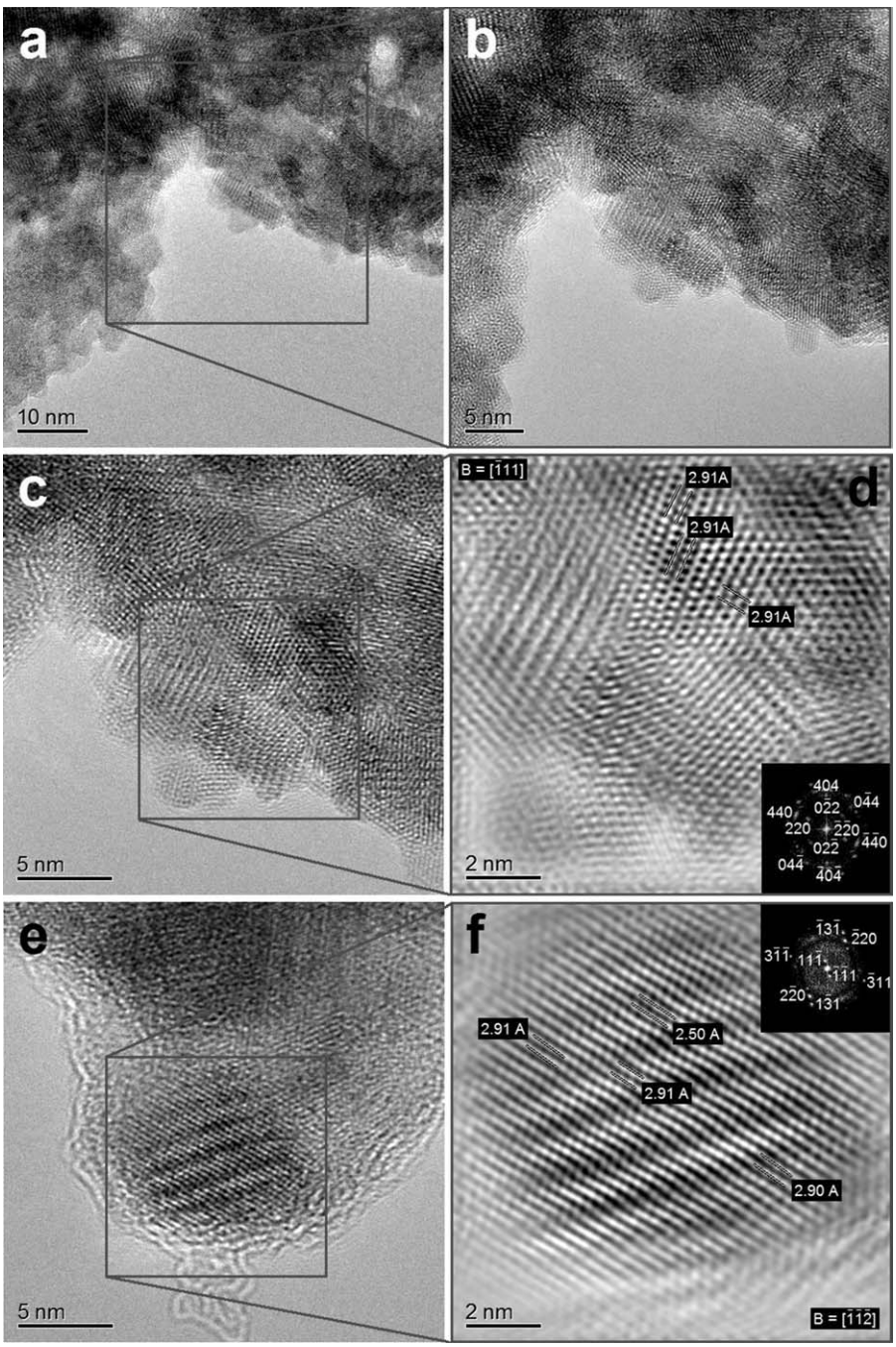

Figure 2 HRTEM images of composite samples: (a) nanoparticles from a 50/50CCF sample, (b) magnification of the indicated area in part a, (c) magnification of part b, (d) Fourier transform filter image of the indicated area in part c, (e) nanoparticle from a 25/75CCF sample, and (f) Fourier transform filter image of the indicated area in part e. The insets in parts d and f show corresponding indexed Fourier transform patterns. Parameter *B* indicates the crystalline direction of the image to which the electron beam is parallel.

which produced frustration over the spin moment relaxation alignment to the applied field. Nevertheless, the high coercitivity values and low remanence ratios strongly suggested that the particles in both samples possessed uniaxial anisotropy.[36–38] There is also a noticeably rapid decay of the remanence at low magnetic fields. This steplike change has previously been attributed to interparticle interactions, which conduces to a frustrated magnetic response of the particle magnetic moment to the applied field, when there is a change on its direction.[36,38] Moreover, both samples showed a significantly reduced magnetization saturation value with respect to the bulk cobalt-ferrite (94 A m^2/kg).[34,38,39] It has been reported that this reduction can be associated with magnetic frustration over the interactions between a

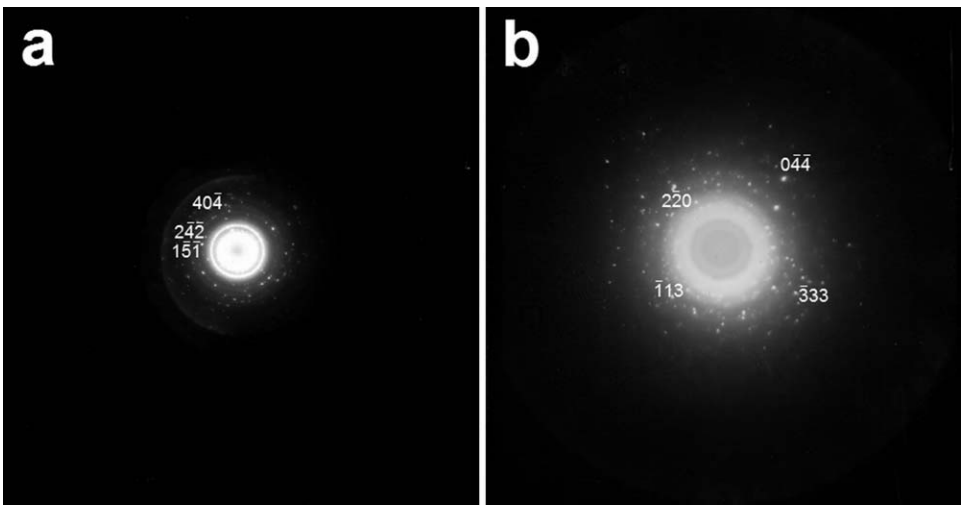

Figure 3 Selected area electron diffraction patterns of (a) 50/50CCF and (b) 25/75CCF, performed with nanobeam diffraction probes of 5 and 2 nm, respectively.

magnetic disordered phase on a surface layer of the particles (e.g., spin-glass ordering) and its magnetically ordered core.[39,40] These intraparticle interactions are clearly shown in Figure 5, where the aforementioned $M(H)$ hysteresis loops at 1.8 K are compared with those obtained after a field-cooled (FC) process at 7 T. There is a noticeable shift in the hysteresis loops of both samples, which indicates a preferred orientation of the magnetic moment of the particles. The field offset from the origin of the hysteresis graph is called the *exchange anisotropy field.* This offset is associated with a preferred magnetic orientation imposed upon a surface magnetic disordered phase during the FC process. Once the magnetic field is removed, the ordered magnetic core is oriented by the frozen surface layer field in the direction of the previously applied field. The values of the exchange anisotropy field for the samples 25/75CCF and 50/50CCF were 0.32 and 0.31 T, respectively.

Figure 6 shows the evolution of the coercitivity (H_c) as a function of the temperature of the 25/75CCF and 50/50CCF samples. In both samples, there was a remarkable decay of the coercivity at 100 K, which suggested that this temperature was the threshold of the superparamagnetic relaxation of both magnetic systems. Superparamagnetic relaxation occurs at a temperature at which the particle moment relaxation time equals the measurement time. This critical temperature is known as the *blocking temperature.* Accordingly, Figure 7 shows the temperature-dependent magnetization [$M(T)$] measure of both samples, showing the correspondent ZFC and FC curves obtained at 10 mT. As it is noticeable, the ZFC curves exhibit a maximum attributed to the blocking temperature, which occurred at

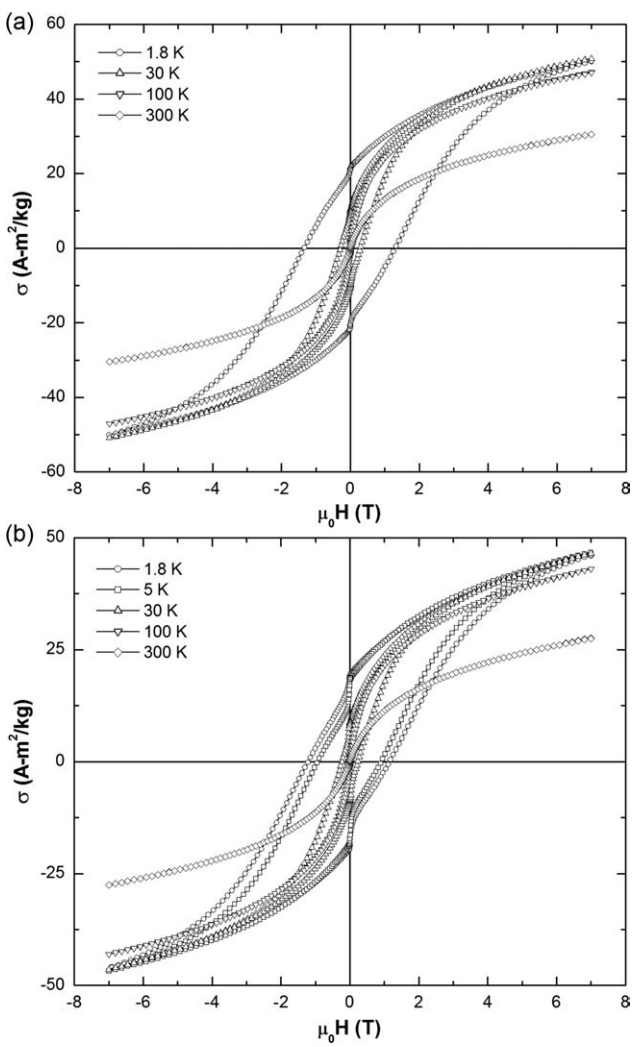

Figure 4 $M(H)$ hysteresis loops of (a) 50/50CCF and (b) 25/75CCF obtained after a ZFC process at the indicated temperatures.

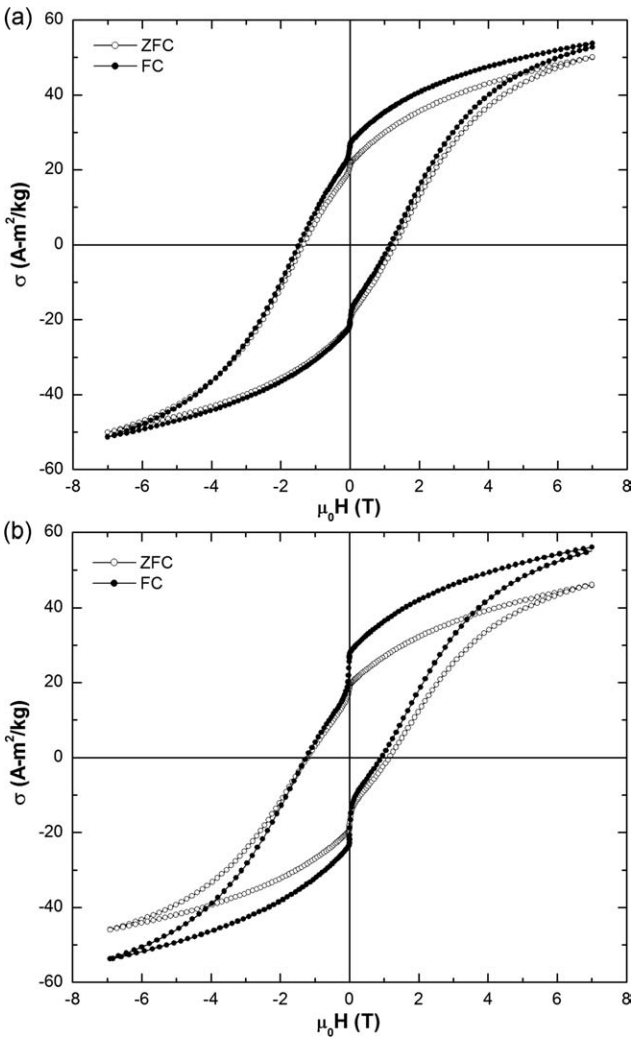

Figure 5 $M(H)$ hysteresis loops of (a) 50/50CCF and (b) 25/75CCF obtained after (○) ZFC and (●) FC processes at 1.8 K.

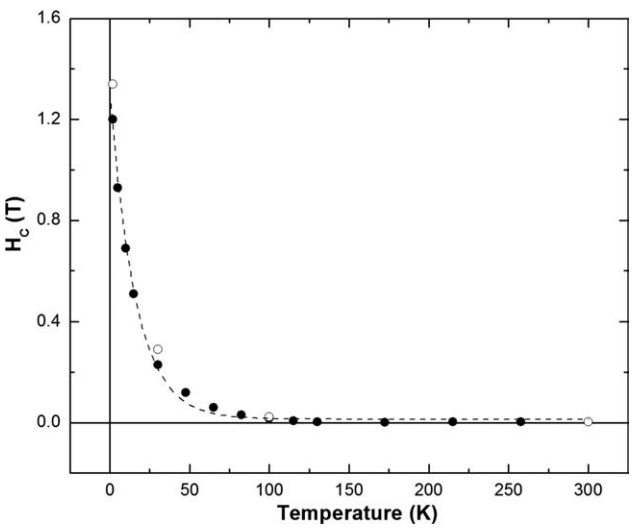

Figure 6 Evolution of the coercivity as a function of temperature for (○) 50/50CCF and (●) 25/75CCF. The dashed line is only a visual guide.

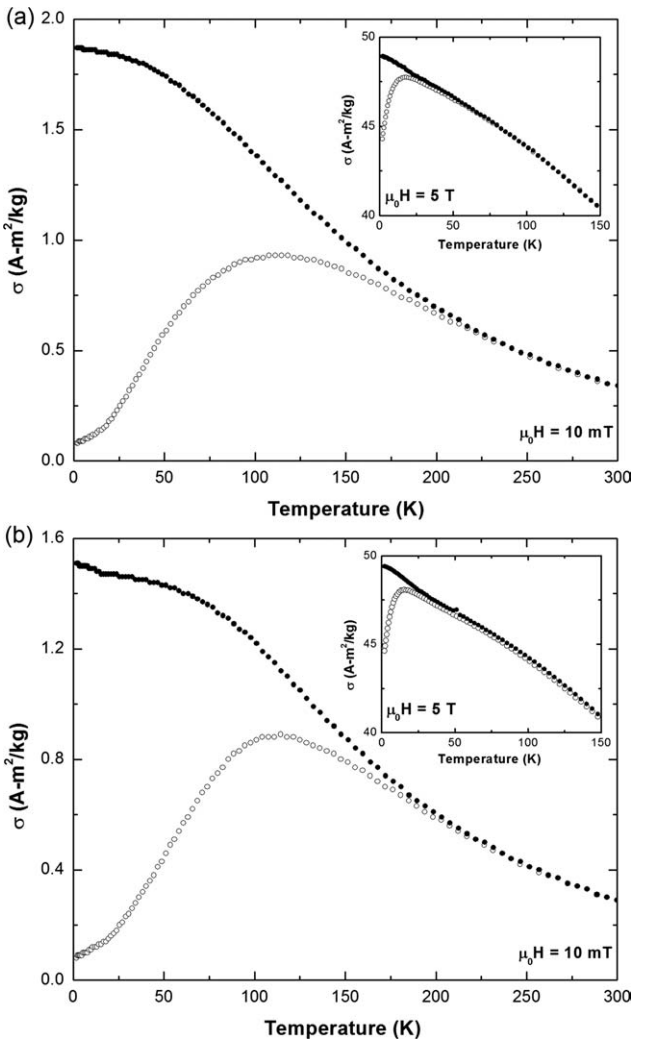

Figure 7 $M(T)$ curves obtained for (○) ZFC and (●) FC processes for (a) 50/50CCF and (b) 25/75CCF with an applied field of 10 mT. The insets show the corresponding ZFC and FC curves obtained with an applied field of 5 T.

107 and 111 K for 25/75CCF and 50/50CCF, respectively, as the curve of the evolution of H_c suggested (see Fig. 6). In addition, there was a significant irreversibility between the ZFC and FC curves, which remained, as the insets shows, at magnetic fields as high as 5 T. First, the low-field irreversibility between the ZFC and FC curves were understood as the ferromagnetic response of blocked magnetic moments aligned with the applied field cooled. Nevertheless, the irreversibility remained at high magnetic fields, which suggest that it could be associated with a freezing process of a magnetic disorder phase.[40]

In addition, it has been reported that it is possible to determine the particle size from the initial magnetization data of magnetic particles over the superparamagnetic regime.[41–43] This approach involves the use of high-field magnetization data, a high-field expansion of the Langevin function, and the

assumption of a log-normal distribution of the particle diameters; then, with eqs. (2)–(7), the following can be calculated:[42] the volume-average diameter corresponding to the mean crystal volume ($\overline{d}_v$), the diameter corresponding to the surface-area-average diameter ($\overline{d}_a$), the log-normal distribution standard deviation (σ_d), the median diameter (d_m), the number-average diameter ($\overline{d}_n$), and the volume-weighted average diameter ($\overline{d}_{vv}$). $\overline{d}_v$ is calculated as follows:

$$\overline{d}_v = \left[\frac{6k_BTM_0}{\pi M_S C_1}\right]^{\frac{1}{3}} \quad (2)$$

where C_1 and M_0 are the slope and linear extrapolation to an infinite field, respectively, from a plot of the observed magnetization ($\mu A–m^2$) versus the inverse field (T^{-1}); k_B is Boltzmann's constant; and T is the temperature at which the measurement was performed. The saturation magnetization per unit of volume of the crystals present in the sample (M_S) were calculated as the ratio of M_0 to ε, where ε is the crystalline volume fraction, which can be evaluated from the cobalt–ferrite content and its density (5.3 g/cm^3):

$$\overline{d}_a = \left[\frac{6k_BT}{\pi M_S}\sqrt{\frac{3\chi}{\mu_0 C_1}}\right]^{\frac{1}{3}} \quad (3)$$

where χ is the initial susceptibility (m^3/kg) evaluated from the magnetization curve as the slope at zero magnetic field:

$$\sigma_d = \exp\left[\sqrt{\frac{2}{3}\ln\left(\frac{\overline{d}_a}{\overline{d}_v}\right)}\right] \quad (4)$$

$$d_m = \overline{d}_v \exp\left[-\frac{3}{2}(\ln\sigma_d)^2\right] \quad (5)$$

$$\overline{d}_n = \overline{d}_v \exp\left(-(\ln\sigma_d)^2\right) \quad (6)$$

$$\overline{d}_{vv} = \overline{d}_v \exp\left(2(\ln\sigma_d)^2\right) \quad (7)$$

These calculations were performed with the initial magnetization data, obtained from 6 to 7 T at 300 K. The results of the calculations are summarized in Table III. As is noticeable, there was quite close correspondence with those particle sizes obtained by the XRD and HRTEM techniques; the quite small deviations of the particle size obtained from this approach were related to the presence of the disordered magnetic phase that surrounded the magnetic ordered core of the cobalt–ferrite nanoparticles.[35] Moreover, these results indicate that the particle size was independent of the concentration of the nanoparticles, even at a cobalt–ferrite concentration of 75% w/w, and also depict a narrow particle size distribution.

TABLE III
Particle Size Distributions Calculated from the Initial Magnetization Data for Each Sample

Sample	$\overline{d}_v$ (nm)	$\overline{d}_a$ (nm)	σ_d	d_m (nm)	$\overline{d}_n$ (nm)	$\overline{d}_w$ (nm)
25/75CCF	2.74	3.24	1.40	2.31	2.45	3.43
50/50CCF	2.80	3.36	1.42	2.33	2.48	3.57

CONCLUSIONS

In this article, we presented a one-step procedure for the synthesis of chitosan/cobalt–ferrite composites, with which it was possible to reach narrow particle size distribution, even at a nanoparticle concentration of 75% w/w. As the XRD, HRTEM, and magnetic measurements techniques suggested, the use of polymeric films of transition-metal ions chelates, such as Co(II) and Fe(III), as starting materials, assured stable particles sizes, which seemed to be independent of the particle concentration. Moreover, the magnetic measurements demonstrated that the synthesized magnetic composites depicted superparamagnetic relaxation above their corresponding blocking temperature (≈110 K) and that there was also present a significant magnetic frustration on the particle magnetic moment alignment, induced by both interparticle and intraparticle interactions.

References

1. Becker, C.; Hodenius, M.; Blendinger, G.; Sechi, A.; Hieronymus, T.; Muller-Schulte, D.; Schmitz-Rode, T.; Zenke, M. J Magn Magn Mater 2007, 311, 234.
2. Steinke, F.; Andrä, W.; Heide, R.; Werner, C.; Belleman, M. E. J Magn Magn Mater 2007, 311, 216.
3. Bo, Z.; Jianmin, X.; Huizhou, L. Front Chem Eng Chin 2007, 1, 96.
4. Rana, S.; Gallo, A.; Srivastava, R. S.; Misra, R. D. K. Acta Biomater 2007, 3, 233.
5. Nikitin, P. I.; Vetoshko, P. M.; Ksenevick, T. I. J Magn Magn Mater 2007, 311, 445.
6. Mirowski, E.; Moreland, J.; Russek, S.; Donahue, M.; Hsieh, K. J Magn Magn Mater 2007, 311, 401.
7. Fernández-Pacheco, R.; Marquina, C.; Valdivia, J. G.; Gutiérrez, M.; Romero, M. S.; Cornudella, R.; Laborda, A.; Viloria, A.; Higuera, T.; García, A.; García de Jalón, J. A.; Ibarra, M. R. J Magn Magn Mater 2007, 311, 318.
8. Shultz, M. D.; Calvin, S.; Fatouros, P. P.; Morrison, S. A.; Carpenter, E. E. J Magn Magn Mater 2007, 311, 464.
9. Mishima, F.; Fujimoto, S.; Takeda, S.-I.; Izumi, Y.; Nishijima, S. J Magn Magn Mater 2007, 310, 2883.
10. Leslie-Pelecky, D. L.; Rieke, R. D. Chem Mater 1996, 8, 1770.
11. Novak, M. A.; Folly, W. S. D.; Sinnecker, J. P.; Soriano, S. J Magn Magn Mater 2005, 294, 133.
12. Trohidou, K. N.; Vasilakaki, M.; Del Bianco, L.; Fiorani, D.; Testa, A. M. J Magn Magn Mater 2007, 316, e82.
13. Widatallah, H. M.; Al-Omari, I. A.; Sives, F.; Sturla, M. B.; Stewart, S. J. J Magn Magn Mater 2008, 320, e324.

14. Bakar, M. A.; Tan, W. L.; Bakar, N. H. H. A. J Magn Magn Mater 2007, 314, 1.
15. Sunkara, B. K.; Misra, R. D. K. Acta Biomater 2008, 4, 273.
16. Baldi, G.; Bonacchi, D.; Innocenti, C.; Lorenzi, G.; Sangregorio, C. J Magn Magn Mater 2007, 311, 10.
17. Ayala-Valenzuela, O.; Fannin, P. C.; Betancourt-Galindo, R.; Rodríguez-Fernández, O.; Matutes-Aquino, J. J Magn Magn Mater 2007, 311, 111.
18. Chen, Z.; Gao, L. Mater Sci Eng B 2007, 141, 82.
19. Pradhan, P.; Giri, J.; Banerjee, R.; Bellare, J.; Bahadur, D. J Magn Magn Mater 2007, 311, 208.
20. García-Cerda, L. A.; Escareño-Castro, M. U.; Salazar-Zertuche, M. J Non-Cryst Solids 2007, 353, 808.
21. Rajan, G. S.; Stromeyer, S. L.; Mauritz, K. A.; Miao, G.; Mani, P.; Shamsuzzoha, M.; Nikles, D. E.; Gupta, A. J Magn Magn Mater 2006, 299, 211.
22. Shchukin, D. G.; Radtchenko, I. L.; Sukhorukov, G. B. J Phys Chem B 2003, 107, 86.
23. Yang, K.-K.; Wang, X.-L.; Wang, X.-L. J Ind Eng Chem 2007, 13, 485.
24. Kim, E. H.; Ahnb, Y.; Lee, H. S. J Alloys Compd 2007, 434, 633.
25. Donadel, K.; Felisberto, M. D. V.; Fávere, V. T.; Rigoni, M.; Batistela, N. J.; Laranjeira, M. C. M. Mater Sci Eng C 2008, 28, 509.
26. Kim, E. H.; Lee, H. S.; Kwak, B. K.; Kim, B. K. J Magn Magn Mater 2005, 289, 328.
27. Lee, H. S.; Shao, H.; Huang, Y.; Kwak, B. K. IEEE Trans Magn 2005, 41, 4102.
28. Lee, H. S.; Kim, E. H.; Shao, H.; Kwak, B. K. J Magn Magn Mater 2005, 293, 102.
29. Zhu, A.; Yuan, L.; Liao, T. Int J Pharm 2008, 350, 361.
30. Li, B.; Jia, D.; Zhou, Y.; Hu, Q.; Cai, W. J Magn Magn Mater 2006, 306, 223.
31. Qiao-Ling, H.; Jia, W.; Fu-Ping, C.; Jia-Cong, S. Chem Res Chin Univ 2006, 22, 792.
32. Onsoyen, E.; Skaugrud, O. J Chem Technol Biotechnol 1990, 49, 345.
33. Schmuhl, R.; Krieg, H. M.; Keizer, K. Water SA 2001, 27, 1.
34. Jin, L.; Bai, R. Langmuir 2002, 18, 9765.
35. López, J. L.; Pfannes, H.-D.; Paniago, R.; Sinnecker, J. P.; Novak, M. A. J Magn Magn Mater 2008, 320, e327.
36. Maaz, K.; Mumtaz, A.; Hasanain, S. K.; Ceylan, A. J Magn Magn Mater 2007, 308, 289.
37. Ammar, S.; Helfen, A.; Jouini, N.; Fievet, F.; Rosenman, I.; Villain, F.; Molinie, P.; Danot, M. J. Mater Chem 2001, 11, 186.
38. Calero-Ddelc, V. L.; Rinaldi, C. J Magn Magn Mater 2007, 314, 60.
39. Sato Turtelli, R.; Duong, G. V.; Nunes, W.; Grössinger, R.; Knobel, M. J Magn Magn Mater 2008, 320, e339.
40. Martinez, B.; Obradors, X.; Balcells, L.; Rouanet, A.; Monty, C. Phys Rev Lett 1998, 80, 181.
41. Jung, C.; Jacobs, P. Magn Reson Imaging 1995, 13, 661.
42. Sjögren, C.; Johansson, C.; Naevestad, A.; Sotum, P. C.; Briley-Saebo, K.; Fahlvik, A. K. Magn Reson Imaging 1997, 15, 55.
43. Li, B.; Jia, D.; Zhou, Y.; Hu, Q.; Cai, W. J Magn Magn Mater 2006, 306, 223.